Brazilian Journal of Physics (2023) 53:91
https://doi.org/10.1007/s13538-023-01300-1

SOCIEDADE BRASILEIRA DE FÍSICA

CONDENSED MATTER

Influence of Er/Fe Substitution on Mg-Zn Nanoparticles' Electromagnetic Properties and Applications

Banoth Baburao[1] · N. Hari Kumar[2] · Avula Edukondalu[1,3] · D. Ravinder[1]

Received: 14 February 2023 / Accepted: 14 April 2023 / Published online: 16 May 2023

Abstract

$Mg_{0.8}Zn_{0.2}Er_xFe_{2-x}O_4$ (x = 0.00, 0.005, 0.01, 0.015, 0.02, and 0.025) nanoparticles made using the citrate gel autocombustion process were examined for their structure, morphology, and behavior. The single-phase cubic spinel structure was formed according to the diffraction pattern. Observations revealed that as the Er focus went from to 0.0 to 0.025, the average crystallite size (*D*) increased from 12.4 to 18.6 nm. The findings of the SEM and EDAX analyses reveal that the particles are uniform, with just a little amount of agglomeration and no impurity pickup. Nanoparticles from transmission electron microscopes (TEM) were present, the range from 12 to 19 nm. In IR spectroscopy using the Fourier transform (FTIR), nearly all the spinel ferrites presented generate two absorption bands that have wavelengths of around 400 cm and 600 cm. The BET surface area of the Er^{3+} ion doping Zn-Mg ferrites rises from 23.860 m^2/gm to 29.845 m^2/gm. The TG–DTA analysis of the prepared samples confirms the thermal stability of the samples; the temperature ranges from 100 to 750 °C.The transition temperature (Seebeck coefficient) of the samples was studied using thermoelectric power (TEP) measurement studies, and it was found that all the samples showed N-type semiconductor behavior. With an increase in erbium concentration, DC conductivity decreases. At room temperature, the magnetic characteristics of hysteresis loops, squareness ratio (SQR), anisotropy constant (K), magnetic moment (), coercivity (Hc), saturation magnetization (Ms), and retentivity (Mr) were examined. When erbium concentration rises, the magnetic moment (B) increases. The saturation magnetization values were 288.4615 and 244.5266 emu/g, and squareness ratio values from 0.01554 to 0.03303 were observed. These materials are converted from hard permanent magnet materials to soft magnet materials.

Keywords Nanoparticles · Structural studies · Electrical transport properties · Magnetic properties

1 Introduction

Spinel ferrites have typically been employed in a variability of magnetic devices, including energy plants, electronic and electrical devices, and magnetic heads in high-density audio and video recording mediums. Some specific medical applications for ferrite nanoparticles include magnetically guided medicine delivery, MRI (magnetic resonance imaging), and medical diagnostics. Electric, magnetic, and catalytic capabilities are only a few of the numerous typical characteristics that ferrites possess. The purification of histidine-tagged proteins in biological systems is another cancer treatment important advantage [1, 2]. They have a low DC because of electrical resistivity and magnetic coercivity; ferrites have significant importance for applications in magnetic memory, high-frequency electronics, detection of COVID-19, and other devices [3-5].

Magnesium cations (mg^{2+}) frequently prefer octahedral(B) sites in the context of magnesium zinc iron oxide inverse spinel structure [6-8]. However, the ferric ions (Fe^{3+}) have a strong predilection for the tetrahedral (A) sites. The magnesium ferrites (MF) and MFs-based materials, on the other hand, were especially restricted to prospective microwave device applications, such as circulating systems, antennas, electrodes, and magnetic hyperthermia applications [9, 10],

✉ N. Hari Kumar
namaharikumar@gmail.com

✉ D. Ravinder
ravindergupta28@rediffmail.com

[1] Department of Physics, University College of Science, Osmania University, Hyderabad, India 20

[2] Department of Physics, St. Mary's Group of Institutions, Deshmukhi, Yadadri Bhongiri, India 508116

[3] Department of Physics, University Post Graduate College, Osmania University, Secunderabad, India 500003

due to their Curie temperature (Tc), modest electrical conductivity value, saturation magnetization that is high (Ms), other magnetic fields with little loss features, and biomedical applications [11-15].

Ferrites might be made using a number of different processes, including microwave hydrothermal [16], flash combustion [17], co-precipitation [18], sol–gel, and citrate gel techniques [19-21]. Comparing all of such synthesis techniques, the citrate gel autocombustion method emerged as the most appealing due to its use of low operating temperatures, quick reaction times, homogeneous material mixtures, small (nano)sized particles, etc. [22, 23]. Since rare earth ions have greater ionic radii than Fe^{3+}, they replace Fe^{3+} in ferrite and diminish the solubility of the spinel lattice [24]. It has been observed that rare-earth ions are viable additives for enhancing the magnetic properties of ferrite.

Rahaman and colleagues [25] investigated Mg-Zn ferrite samples. The surface appearance, crystalline compositions, and microwave properties of the proposed Flexible composites using Mg-Zn ferrite as their foundation investigated using field emission scanning electron microscopy (FESEM), X-ray diffraction (XRD), and a dielectric assessment kit (DAK). AmnaIrshad et al. [26] studied structural and photocatalyst studies of co-substituted Mg-Zn spinel nanocrystalline ferrites. Tholkappiyan et al. [27] observed that structural, optical, and magnetic properties were synthesized by the combustion method with the use of glycine as fuel. Ali et al. [28] studied the Yttrium-(Y) substituted Mg-Zn structural, electrical, dielectric, and magnetic characteristics of ferrites. It is a new compositional investigation that is now being studied Er Substituted Mg-Zn nanoferrites, and getting dynamic results requires interpretation.

The electrical, magnetic, structural, thermal, and spectroscopic properties of the prepared Er-substituted Mg-Zn nanoferrites have been investigated, as has electrical conductivity in dc. The above-mentioned qualities of the current materials are of interest to the writers.

2 Experimental Studies

2.1 Materials

The following raw materials were chosen for the synthesis of the Er-substituted Mg-Zn ferrite nanoparticles: magnesium nitrate [Mg $(NO_3)_2{\cdot}6H_2O$], zinc nitrate [Zn $(NO_3)_2$ $6H_2O$], erbium nitrate [Er $(NO_3)_3 6H_2O$], ferric nitrate [Fe $(NO_3)_3$ $9H_2O$], and citric acid [$(C_6H_8O_7)$ H_2O].

2.2 Synthesis Method

The aforementioned ingredients were chosen to manufacture the erbium substituted magnesium ferrites nanoparticles. These were weighed in accordance with the calculated metal nitrate stoichiometric ratio. Additionally, distilled water was used to dissolve these chemicals. In order to accomplish the citrate gel autocombustion technique, citric acid was present in the nitrate compounds, then combined based on the molar ratio. The heated plate is on a magnetic stirrer; the stirring lasted about an hour. The p_H level was maintained at 7 by gradually introducing the ammonia solution. This led to the creation of the dry gel. This fragment was subjected to further autocombustion to produce ferrite powder particles. Additionally, a powder sample was ground and further described utilizing a variety of characterization methods. For structural analysis, the X-ray diffraction, two probes for scanning and measurement, measurement of the LCR, and electron transmission microscopy are used, respectively. Tristar 3000 BET surface analyzer (Micromeritics) and Thermo gravimetric/Differential Thermal Analyzer instruments to find out the BET and TG/DTA characterizations. The process flow diagram for creating the current ferrite materials is displayed in Fig. 1.

3 Results and Analysis

3.1 XRD

X-ray diffraction analysis of Er-substitution Mg-Zn nano ferrite XRD patterns is shown in Fig. 2. In this study, the full prof crystallographic tool was used to examine XRD data with Rietveld refinement. Figure 2b shows the Rietveld refinement pattern. The conception of a well-defined single-phase cubic spinel structure was thought to have been substantiated by the produced samples' diffraction patterns and no secondary peak created [29, 30]. The Debye–Scherrer formulation for calculating crystallite size (d) is as follows:

$$d = \frac{k\lambda}{\beta cos\theta} \tag{1}$$

The "crystallite size" is denoted by the letter "d," the "X-ray wavelength" is denoted by the letter "λ," the "FWHM" is denoted by the letter "β," and the "diffraction angle" is denoted by the letter "θ." By means of the Scherrer formula [31], it was discovered that the produced crystallite dimensions of nanoferrites, as determined from the high intensity peak's half-maximum at its whole breadth (311), ranged between 12.4 and 18.6 nm. The produced Er-substituted Mg-Zn nanocrystalline samples' XRD investigation yielded estimates for the lattice constant (a), average crystallite size (D), X-ray density (dx), and other quantities shown in Table 1 [32-34]. The expression of the lattice constant is as follows:

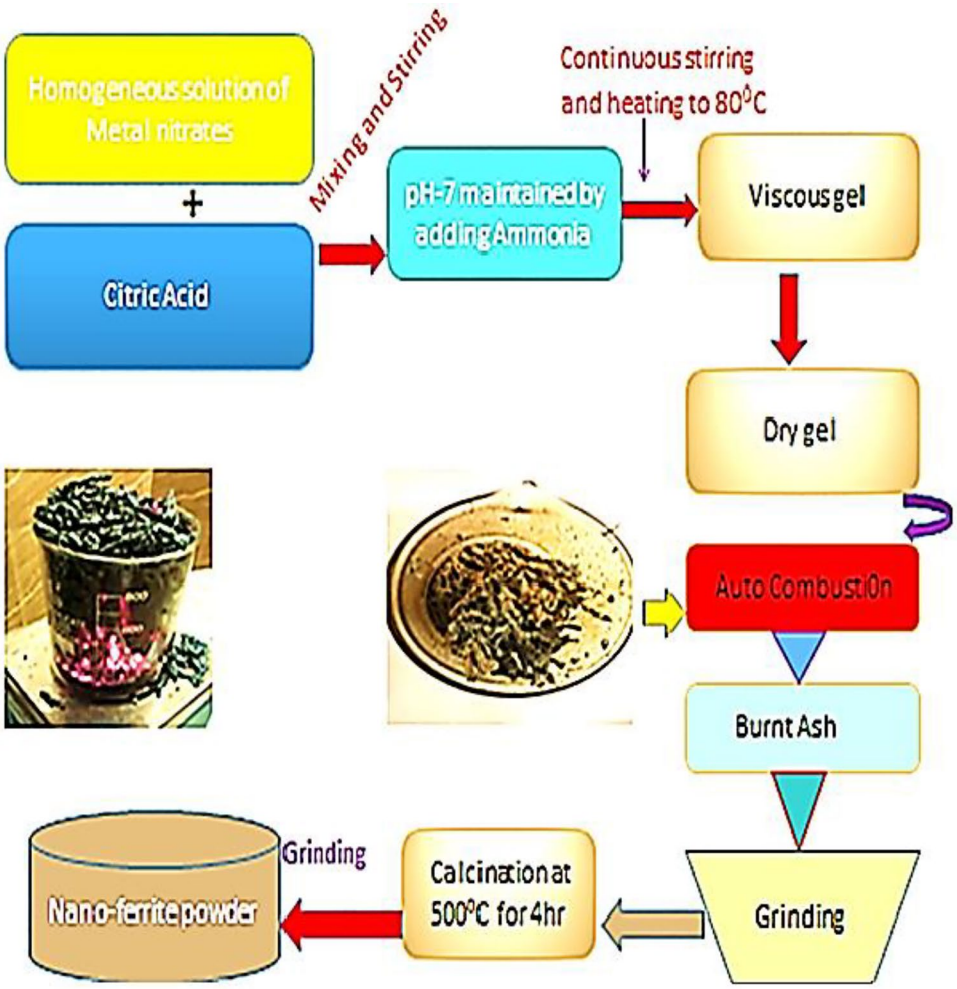

Fig. 1 Synthesis flow chart of Er-substituted Mg-Zn nanoferrites

$$a = d(\sqrt{h^2 + k^2 + l^2}) \tag{2}$$

The "lattice constant" is shown here as "*a*," the "basic lattice's length" is shown as "*d*," and the "Miller indices" are shown as "*h*," "*k*," and "*l*." As the Er-content increased from 0.0 to 0.025, the lattice parameter was seen to drop from 8.46 to 8.38. X-ray density was estimated by the standard formula:

$$d_x = \frac{8M}{N_A a^3} \tag{3}$$

Here, "*M*" represents the "molecular weight" of the corresponding sample. "N_A" is "Avogadro's number," and "*V*" is "cell volume." The X-ray density increased along with the rising dopant concentration. With a rise in Er-content, it was seen that the X-ray density was increasing from 4.58 to 4.67 g/cm^3 [35, 36]. The molecular weight (MW) increased with the addition of a dopant, from 208 to 210 g/mole [37, 38].

3.2 Analysis with SEM and EDS

Figure 3 displays SEM pictures of Er-substituted Mg-Zn ferrites with x = 0.0, 0.005, 0.01, and 0.015. They demonstrate the homogeneity, uniformity, and mild agglomeration of the particles [39]. The form of the components tightly matches those of a compound. They suggest that the substances included sphere-shaped particle forms and constrained sizes of the distributions that were nanoscale in size. The granules are clearly distinct in both compounds, as can be seen. There are not any intra-granular perforations on the surfaces of the grains. The grain shapes will have an impact on the physical aspects. The grains' irregular shapes and orientations are seen in the pictures.

Energy dispersive Spectroscopy is used for the elemental analysis, and Fig. 4 displays the EDS patterns of the nanoferrites under study with x = 0.0, 0.005, 0.01, and 0.015. The only elements present in the EDS patterns, which solely comprise Mg, Zn, Er, Fe, and O, are Mg, Zn, Er, and Fe [40]. The ferrite sample that has been created is flawless and free of any impurities.

3.3 FTIR Analysis

Figure 5 depicts the FTIR spectra for the sample $Mg_{0.8}Zn_{0.2}Er_xFe_{2-x}O_4$ (x = 0.0, 0.005, 0.01, 0.015, 0.02, 0.025) at 0–4500 cm^{-1} frequency range. It comprises two bands (υ_1 and υ_2), with maximal frequencies recorded in the

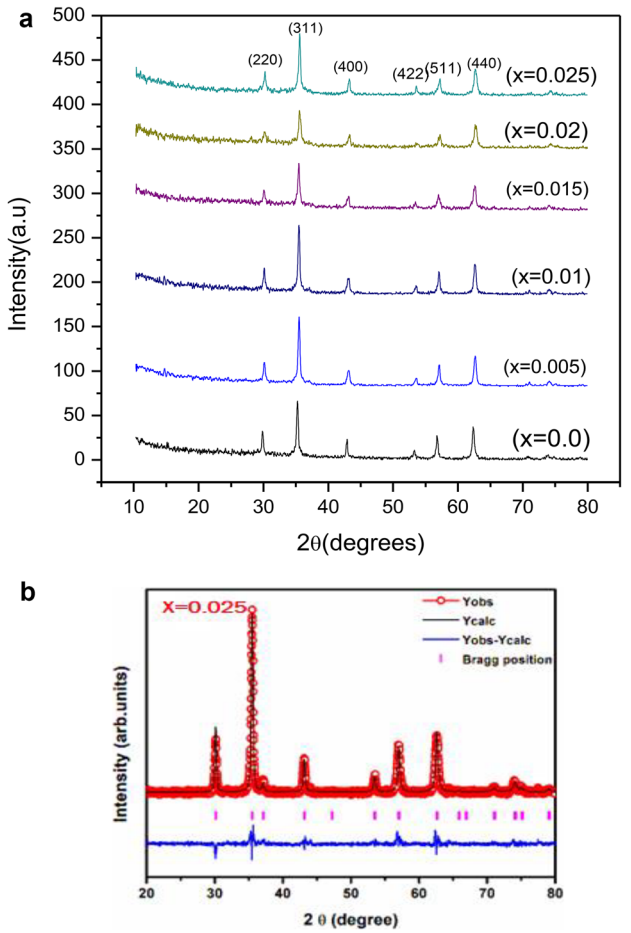

Fig. 2 **a** XRD patterns of Er-substituted Mg-Zn nanoferrites. **b** XRD Rietveld refinement patterns of Er-substituted Mg-Zn (X = 0.025) nanoferrites

550–500 cm^{-1} tetrahedral group and the 450–400 cm^{-1} octahedral group [41]. The effective synthesis of spinel ferrites was validated by the modes of vibration for metal and oxygen found in the vicinity of 600 to 350 cm^{-1} indicated by FTIR spectra. Tetrahedron (Fe–O) FeO_4 stretching vibration modes correspond to a zone of absorption with a higher wave number between 500 and 600 cm^{-1} and the reduced wave number band between 450 and 400 cm^{-1}, as indicated in Table 2 [42]. With increasing concentrations of the Er^{3+} ion in Mg-Zn ferrites, there was a change in the peak position that was observed [43].

The span of the Fe^{3+}tetrahedral and O^{2-} bond has changed. The frequency of the tetrahedral (υ_1) band changed when Er^{3+} ions were present. This shift is caused by the expansion of the A-site, the migration of cations, and changes in bond duration. It also verifies that Er^{3+} ions are present at the A-site [44]. The tetrahedral A-vibrational site's frequency (1) is normally represented by the broad band, whereas the octahedral B-vibrational site's frequency (2) is often represented by the narrow band [32].

The FTIR spectrum analysis typically provides information on the cation attentiveness differential involving sites A and B. The Er^{3+} cations will probably replace the B-Fe^{3+} site's rather than the A-site cations.

3.4 TEM and SAED Analysis

The identical samples' images (TEM and SAED) are shown in Fig. 6a, b. The Er element was added to the magnesium ferrite system, and this caused the formation of well-agglomerated nanoparticles. It was discovered that the typical crystallite size ranged from 12 to 19 nm. This unmistakably demonstrated the wide variations in grain size and particle size [45]. The nanometric range of the particle sizes in the data samples is demonstrated by the TEM micrographs, indicating their nanocrystalline structure. A small number of elongated particles can also be seen in the TEM and SAED (x = 0.005 and 0.025) micrographs, where the majority of the nanoparticles are shown in spherical forms with minuscule thicknesses. For lower replacements of Er^{3+} ions, the particles appear to be effectively separated from one another in TEM images, but when the substitution of Er^{3+} ions rose, the particles developed an agglomerated morphology and started interacting with one another. This outcome shows that the magnetic attraction between these originally stacked nanoparticles is significant. According to TEM micrographs, the usual particle size ranges from 12 to 19 nm.

Table 1 Structural parameters of nanocrystalline Er-substituted Mg-Zn nanoferrites

$Mg_{0.8}Zn_{0.2}Er_xFe_{2-x}O_4$	MW (gm/mole)	Crystallite size (nm)	Lattice parameter (Å)	X-ray density dx (g/cm^3)
0.0	208.207	12.4	8.46	4.58
0.005	208.764	14.1	8.45	4.59
0.01	209.321	15.3	8.42	4.60
0.015	209.878	15.5	8.40	4.62
0.02	210.435	17.6	8.39	4.66
0.025	210.992	18.6	8.38	4.67

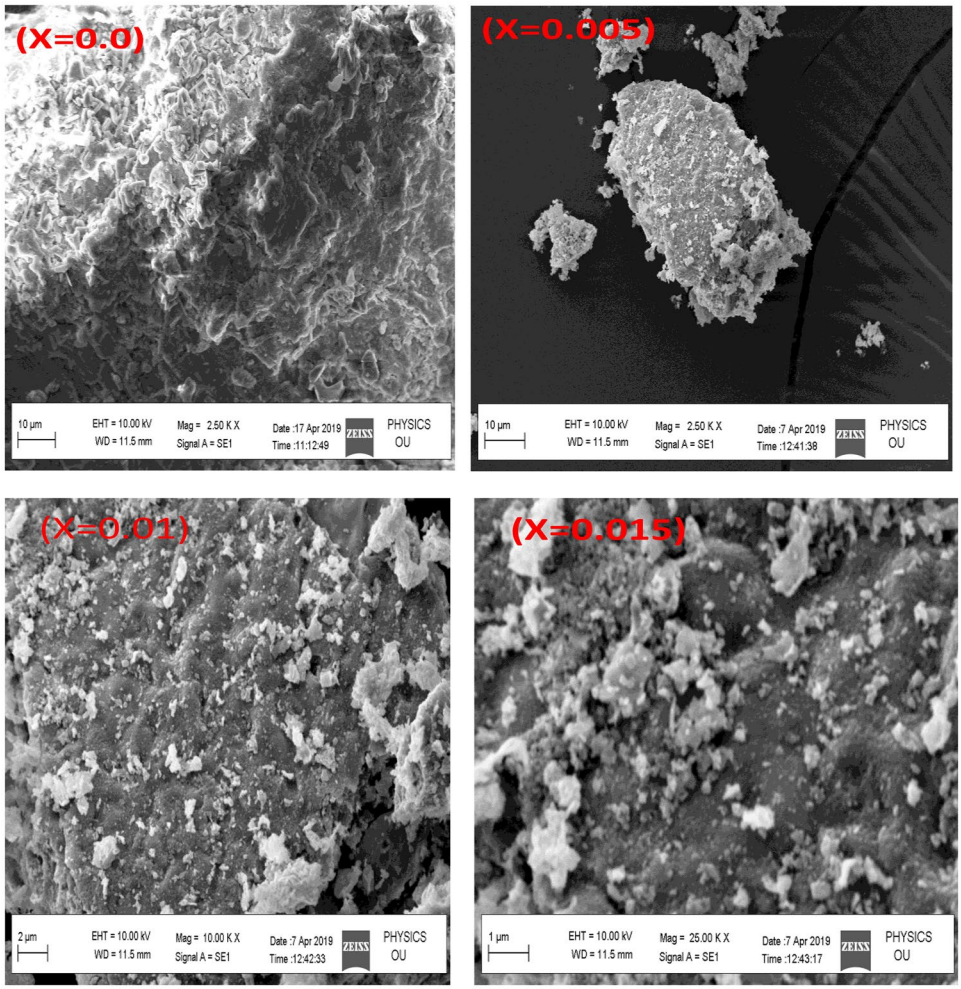

Fig. 3 SEM images of Er-substituted Mg-Zn (x = 0.0, 0.005, 0.01, and 0.015) nanoferrite system

3.5 Surface Analysis (BET)

The specific surface area, macroscopic appearance, and type of nanoscale holes are all essential factors in influencing the surface characteristics of nanoscale materials. The "Brunauer–Emmett–Teller" approach, abbreviated as BET, is extremely beneficial for this purpose. Thus, the BET isotherms for all $Mg_{0.8}Zn_{0.2}Er_xFe_{2-x}O_4$ samples were found in this work. The surface parameter BET surface area was calculated using this physisorption. The BET surface area in Zn-Mg ferrites rises with increasing Er^{3+} ion doping level from 23.860 m^2 /gm to 29.845 m^2 /gm. The found surface area order agrees well with the reported values in previous BET experiments [46]. Figure 7 depicts the composition dependent variation of the BET surface area with increasing Er^{3+} doping level. The increasing trend in BET surface area is consistent with the decrease in average crystallite size estimated by XRD data, as it is well known that the smaller the crystallite size, the larger the surface area.

3.6 TG–DTA Analysis

Thermogravimetric analysis is a technique that measures the mass of a material as a function of temperature or time while subjecting the sample specimen to a controlled temperature program in a controlled environment. DTA measures the temperature of a sample in comparison to a reference material and shown in Fig. 8. Thus, thermogravimetric analysis (TG) evaluates weight changes in a sample, whereas differential thermal analysis (DTA) analyzes temperature variations between a sample and a reference as a function of temperature or time. It should be mentioned that the change from the combustion powder to the final phase occurs in numerous phases. The evaporation of water molecules from the surface is responsible for the first weight loss about 150 °C. At 201 °C, crystallization and breakdown occur. The first weight loss was 20% up to a temperature of roughly 604 °C, accompanied by an exothermic response. This weight loss is mostly due to sample humidity and the presence of water in the erbium nitrate

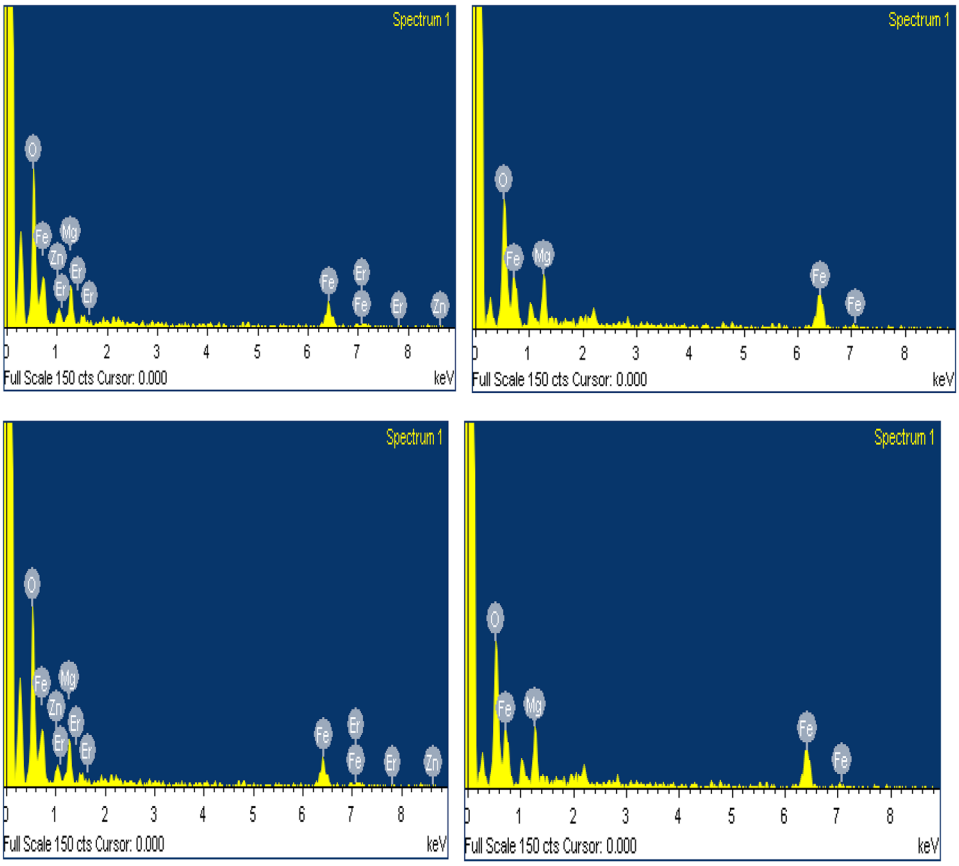

Fig. 4 EDAX patterns of Er-substituted Mg-Zn (x = 0.0, 0.005, 0.01, and 0.015) nanoferrites

and ferric nitrate precursors [29]. Due to the disintegration of erbium contained in the ferrite sample, a further modest weight loss of 80% to 20% is seen in the temperature range 100 °C–750 °C. Finally, no disintegration of the remaining precursors with weight loss was seen above 750 °C, suggesting the development of the $Mg_{0.8}Zn_{0.2}Er_xFe_{2-x}O_4$ structure. XRD and FTIR measurements indicate the production of the $Mg_{0.8}Zn_{0.2}Er_xFe_{2-x}O_4$ ferrite at this temperature.

3.7 DC Electrical Characteristics

3.7.1 Resistivity

Mg-Zn ferrites were reported to have a DC electrical resistivity that ranged from 105 to 109 cm^3 at room temperature [47]. Figure 9 shows the 1000/T vs. log $T\sigma(s/mk)$ DC resistivity graphs, which demonstrate that ferrite samples exhibit a reduction in electrical resistivity with rising temperature. The Arrhenius reference was made to compute the energy of activation for measuring the temperature-dependent DC resistivity of $Mg_{0.8}Zn_{0.2}Er_xFe_{2-x}O_4$ (x = 0.0, 0.005, 0.01, 0.015, 0.02, 0.025) nanoferrites. The samples that had erbium replaced have paramagnetic (Ep) and ferromagnetic (Er) activation energies. For a constant concentration of Mg and Zn ions, the activation energy fluctuates randomly as erbium substitution increases [48]. According to Table 3, the measured Curie temperature was shown to be dropping from 460 to 450 K together with rising erbium concentration.

3.7.2 Conductivity

Erbium-doping Mg-Zn ferrites had an electrical conductivity that varied with temperature, from ambient to considerably over the Curie temperature. Figure 10 shows $T(c)$ vs. $dc(S/m)$ graph is exhibited. The electrical conductivity of Mg-Zn ferrites replaced with erbium varied with temperature, ranging from ambient temperature to properly above the Curie temperature is shown in Fig. 10. Shown is a plot of $T(c)$ versus

Table 2 FTIR vibrational bands of Er-substituted Mg-Zn nanoferrites

$Mg_{0.8}Zn_{0.2}Er_xFe_{2-x}O_4$	Absorption band frequencies (cm^{-1})	
	υ_1	υ_2
0.0	559.5	382.5
0.005	543.5	374.5
0.01	540.3	397.4
0.015	572.7	398.3
0.02	579.1	399.6

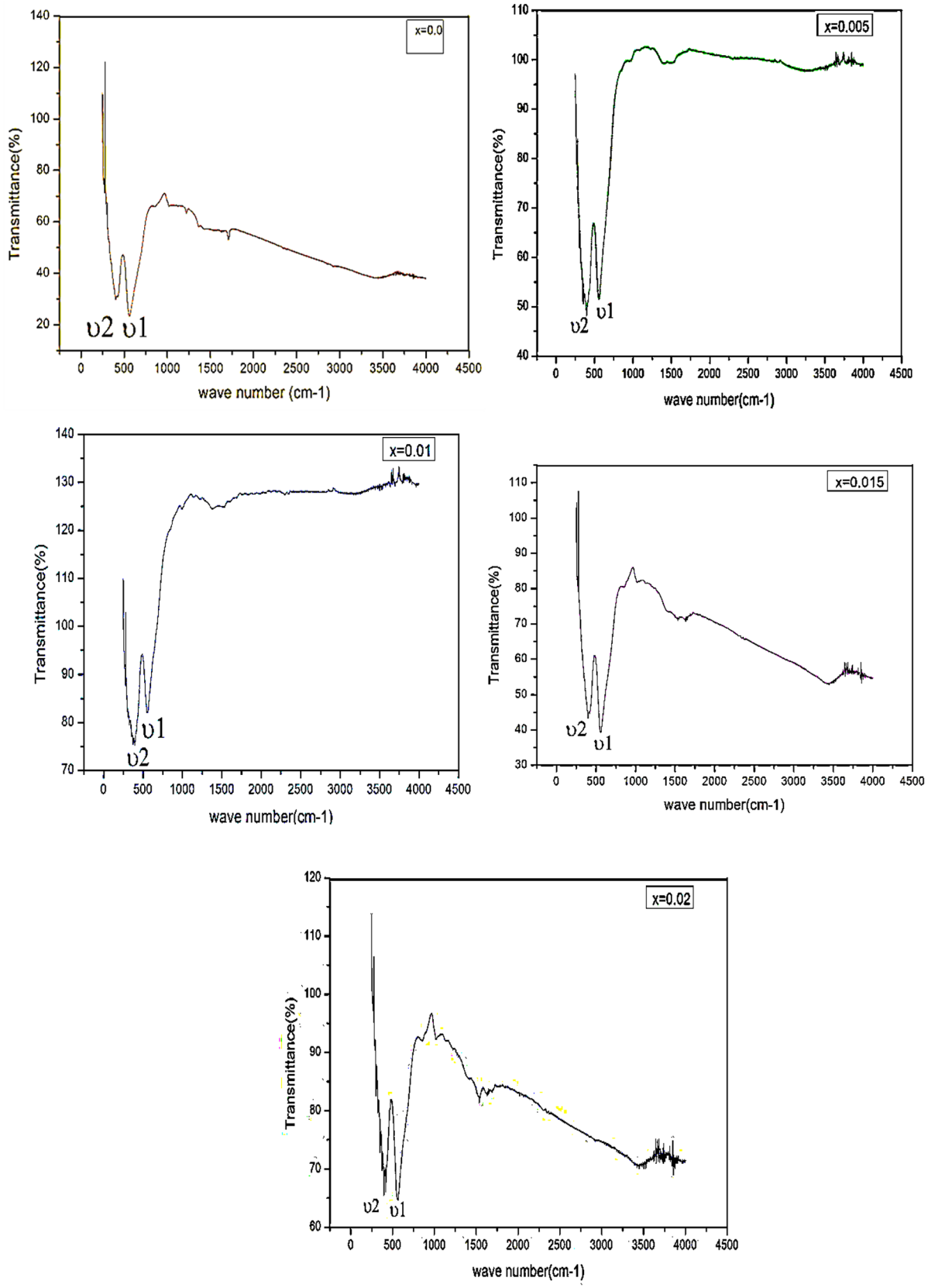

Fig. 5 FTIR spectra of Er-substituted Mg-Zn (x = 0.0, 0.005, 0.01, 0.015, and 0.02) nanoferrites

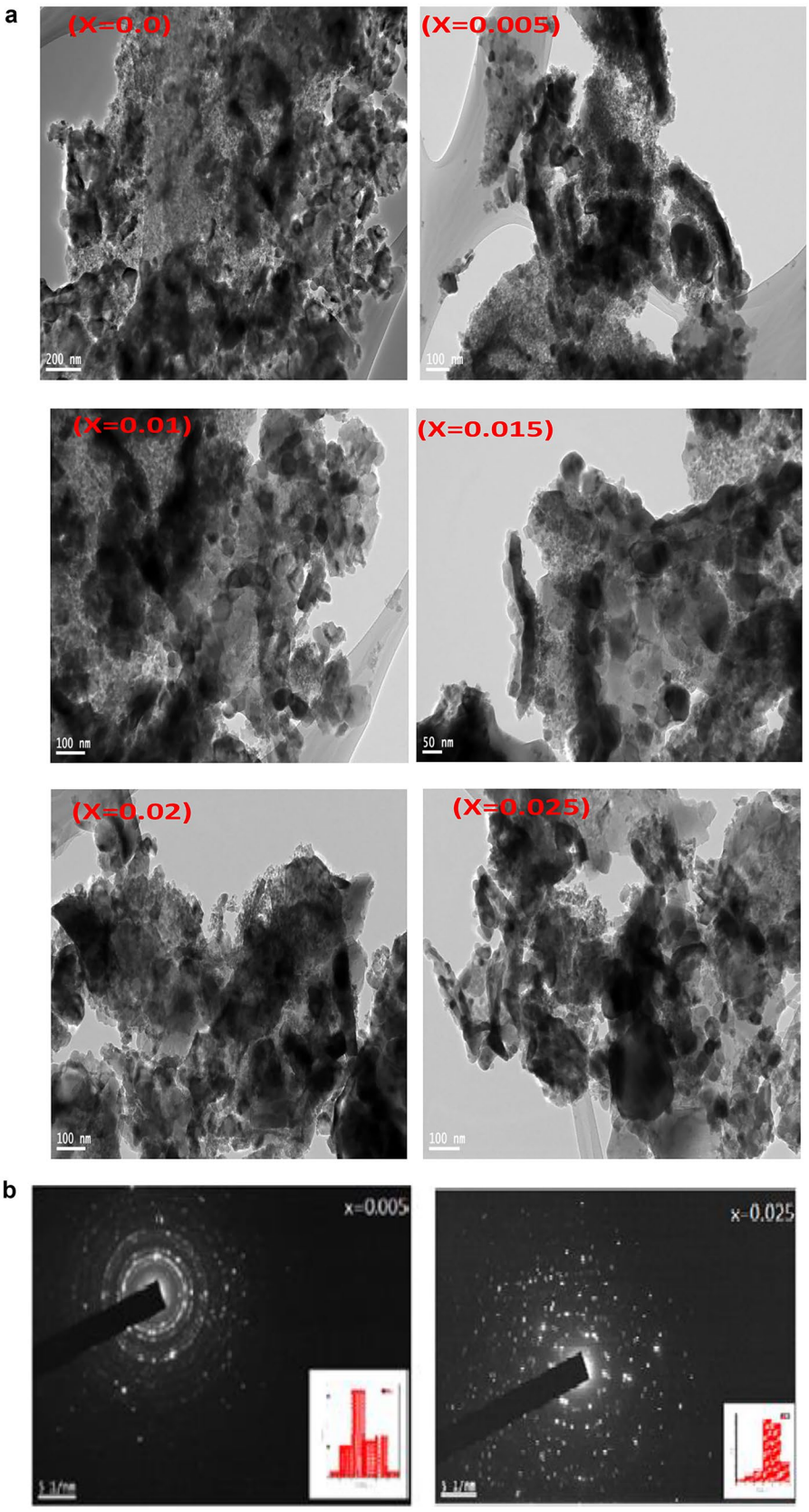

Fig. 6 **a** TEM images of Er-substituted Mg-Zn nanoferrites. **b** SEAD images of Er-substituted Mg-Zn nanoferrites

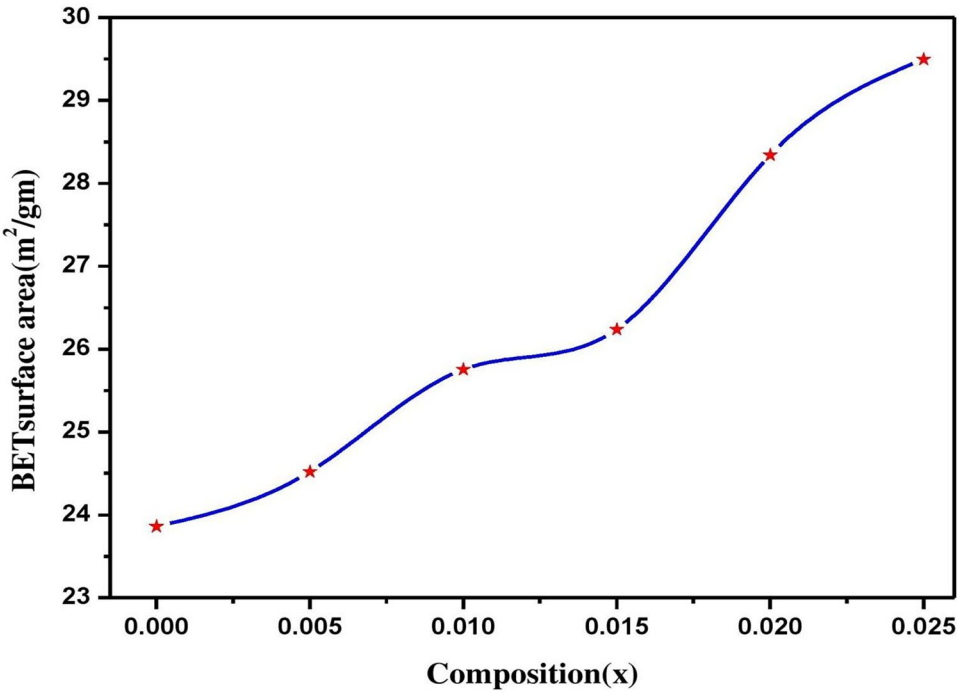

Fig. 7 Variation of BET surface area of Er-substituted Mg-Zn nanoferrites

dc (*S*/*m*). DC conductivity is increased by temperature [49]. With an increase in erbium concentration, DC conductivity decreases. For applications such as thermostats and thermal sensors, the temperature-dependent exponential increase in DC conductivity indicates Curie temperatures resulted in a minor difference in electrical conductivity [50]. Electron hopping between Fe^{2+} and Fe^{3+} is the source of the electrical conductivity seen in $Mg_{0.8}Zn_{0.2}Er_xFe_{2-x}O_4$ (x = 0.0, 0.005, 0.01, 0.015, 0.02, 0.025).

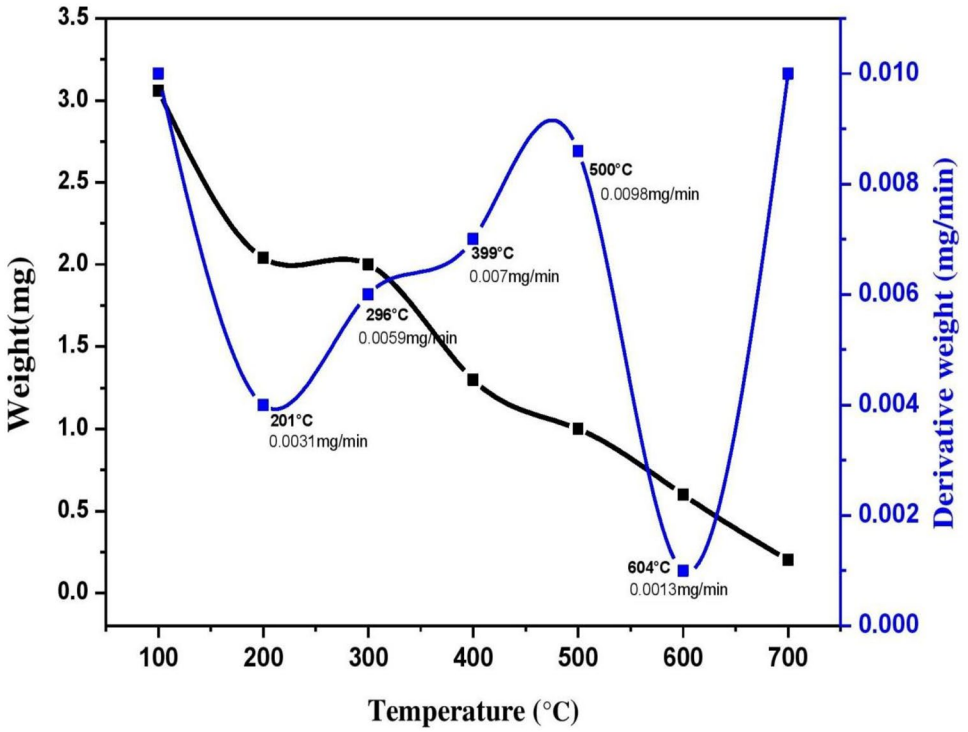

Fig. 8 TG/DTA graph of Er-substituted Mg-Zn nanoferrites

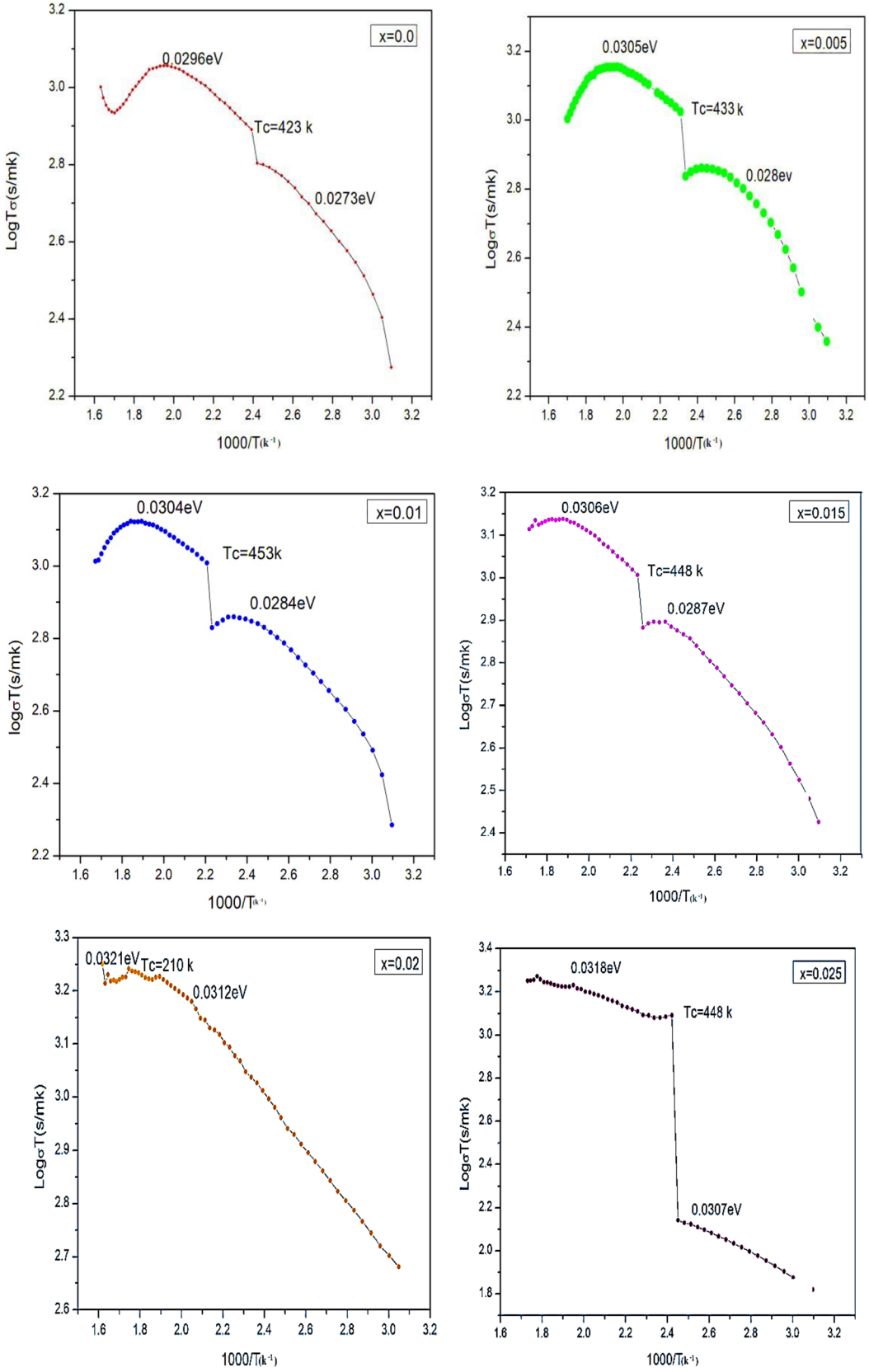

Fig. 9 Variation of dc-resistivity with temperature for Er-substituted Mg-Zn nanoferrites

Table 3 Various DC parameters of Er-substituted Mg-Zn nanoferrites

$Mg_{0.8}Zn_{0.2}Er_xFe_{2-x}O_4$	Curie temperature Tc (K)	Activation energy		
		E_P (eV)	E_F (eV)	ΔE (eV)
0.0	423	0.029	0.027	0.002
0.005	433	0.030	0.028	0.003
0.01	453	0.032	0.029	0.004
0.015	455	0.034	0.033	0.005
0.02	460	0.039	0.038	0.007
0.025	468	0.041	0.040	0.009

3.8 Magnetic Properties

With the aid of a vibrating sample magnetometer with an applied field of H (Oe), at room temperature, the generated samples' magnetic properties were assessed [51]. Figure 11 shows "hysteresis loops" (M-H) of nanoferrites made of $Mg_{0.8}Zn_{0.2}Er_xFe_{2-x}O_4$. M-H loops are often affected by the chemical make-up, the method of synthesis, the size of the crystallites, the borders of the grains, the temperature of sintering, and the distribution of the cations [52]. Table 4 contains the calculated and tabulated values of the erbium-substituted Mg-Zn nanoferrites, as well as the coercivity, residual magnetization (σr), and saturation magnetization (σs), and these values. The following relationships were used to compute at standard temperature, the squareness ratio (SQR), anisotropy constant (*K*), and magnetic moment (B) [53, 54]:

$$\text{Squareness ratio (SQR)} = \frac{\text{Mr}}{\text{Ms}} \tag{4}$$

According to estimated squareness ratio values, the ratio was discovered to change with a rise in erbium concentration, from 0.01554 to 0.03303. Utilizing the following relationships, coercivity is determined:

$$\text{Coercivity (Hc)} = \frac{0.98 * \text{K}}{\text{Ms}} \tag{5}$$

K, in this equation, stands for the anisotropy constant. The fluctuation in crystallite size was seen in the saturation magnetization values, which showed that it initially increases and subsequently declines. The saturation magnetization values were 288.4615 and 244.5266 emu/g, respectively, at their highest and lowest points. The coercivity is low and acts as a generator of a magnetic field when the porosity is large [55].

Soft magnetic substances are widely employed in the windings of motors and transformers, two equipment regularly flip polarity as a result of tiny M-H curve. Soft magnetic substances, as shown below, have little had already lost and remain a significant portion if they pass to zero line at the end of their magnetic field. They also show a high demagnetization slope close to infinity line [56]. Soft

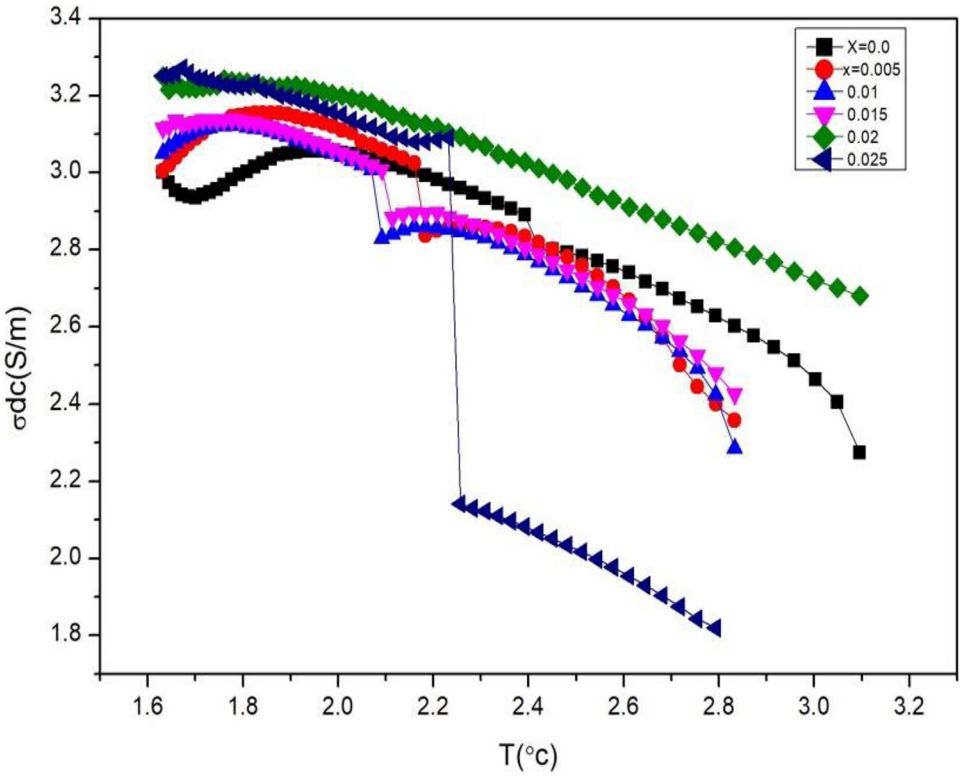

Fig. 10 Variation of dc-conductivity with temperature for Er-substituted Mg-Zn nanoferrites

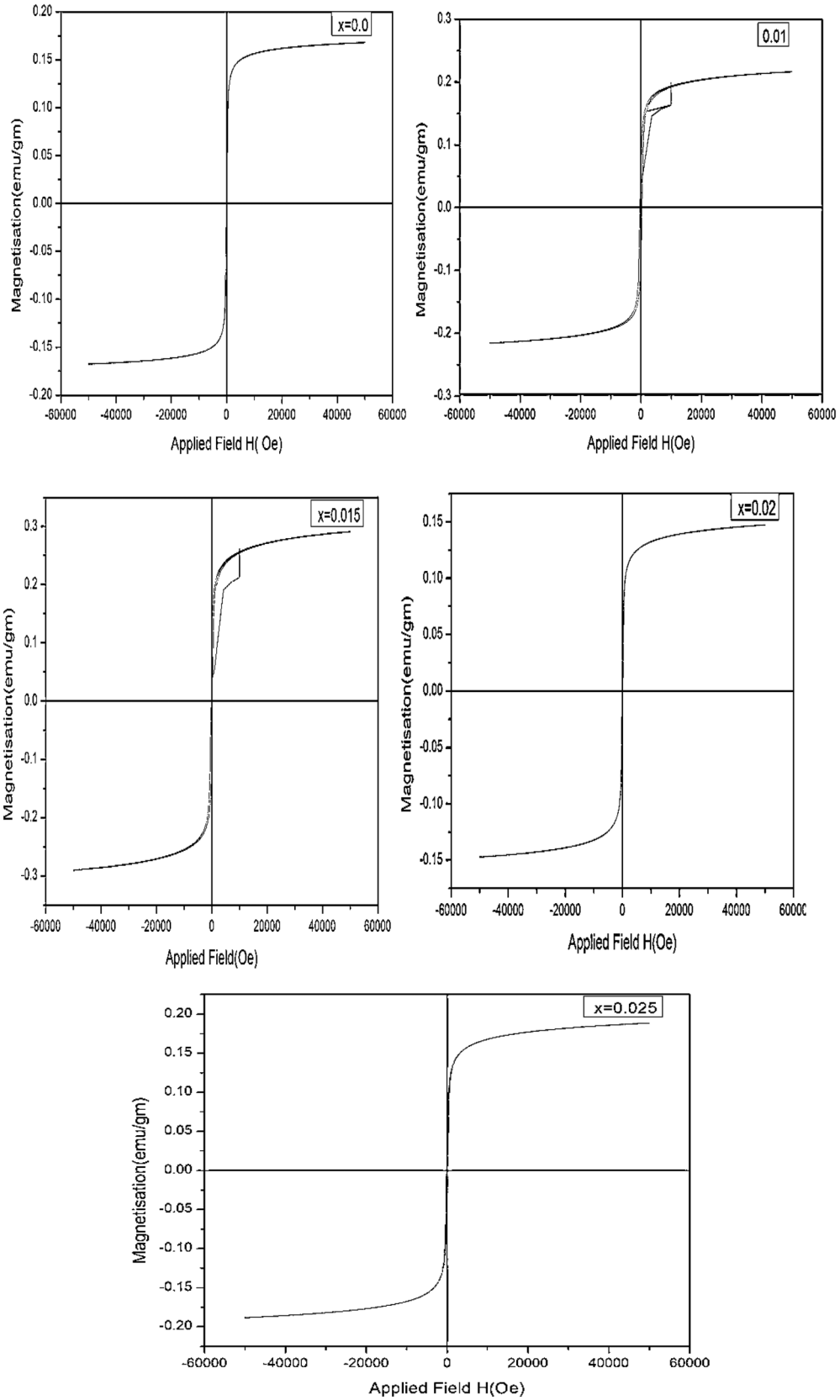

Fig. 11 Hysteresis loops for Er-substituted Mg-Zn (x = 0.0, 0.01, 0.015, 0.02, and 0.025) nanoferrites at room temperature

Table 4 Different parameters of Er substituted Mg-Zn nanoferrites

$Mg_{0.8}Zn_{0.2}Er_xFe_{2-x}O_4$	Saturation magnetization Ms (emu/g)	Remanent magnetization Mr (emu/g)	Coercivity Hc (Oe)	SQR (Mr/M)	Magnetic moment	Anisotropy K*10^3 (erg/cm^3)
0.0	288.4615	4.485	339.733	0.01554	10.7537	0.99
0.01	287.1440	4.5265	341.292	0.02551	10.7619	3.58
0.015	285.7710	4.7727	342.931	0.02670	10.7989	5.98
0.02	271.8389	7.0867	462.615	0.03345	11.9818	6.37
0.025	244.5266	9.3195	516.041	0.03303	31.9049	17.77

magnetic substances may switch polarity more frequently and experience extremely small electrical losses because they apply less pressure. The width of the hysteresis loop reveals important details about the losses [57, 58]. It is not methodical behavior in terms of particle size led to the demonstration of the compositional dependence permeability to magnetic fields [59].

4 Conclusions

The single-phase (spinel structure) Er-substitution nanocrystalline Mg-Zn nanoferrite sample $Mg_{0.8}Zn_{0.2}Er_xFe_{2-x}O_4$ (x = 0.0, 0.005, 0.01, 0.015, 0.02, 0.025) was effectively synthesized in this work using the citrate-gel autocombustion method. Spinel cubic structure in one phase of the materials XRD and FTIR tests provides evidence for this. When Er^{3+} is substituted, the crystallite size of calcinated powders rises and ranges from 96.4 to 144.6 nm. The obtained samples using the SEM method support the presence of aggregated nanoparticles with a spherical form. By using EDX assays, it was proven that ferrite samples included the components Mg, Zn, Er, Fe, and O. The TEM and SAED were used to measure the average particle size. The surface parameter BET surface area was calculated and increases surface area with increasing of Gd^{3+} doping level. From the TG–DTA analysis weight loss of 80% to 20% is seen in the temperature range 100 °C–750 °C. As the temperature rises, the nanoferrites' DC electrical resistance in the papered, pure samples decreases. For every sample of ferrite that was made, the phase variation of $1000/T$ against the log $T\sigma$ (s/mk) graph reveals the Curie point. The energies of activation in ferromagnetic and paramagnetic areas are shown. The electrons in action hopping the relationship between the ions of Fe^{3+} and Fe^{2+} how DC conductivity varied having temperature. The developed materials' ferromagnetic characteristics samples have been verified by the magnetization study performed at room temperature. Ferrites of Er-substituted magnesium and zinc are used in electrical and magnetic fields.

Acknowledgements Thanks are due to SV-TPTY, Head and BOS Department of Physics, University College of Science, Osmania University, Hyderabad.

Author Contribution Banoth Baburao: conceptualization, methodology, data curation, and writing—original draft. N. Hari Kumar: data curation and review and editing. Avula Edukondalu: review and editing. D. Ravinder: supervisor.

Declarations

Ethics Approval We further confirm that any aspect of the work covered in this manuscript that has involved either experimental animals or human patients has been conducted with the ethical approval of all relevant bodies and that such approvals are acknowledged within the manuscript.

Conflict of Interest The authors declare no competing interests.

Declaration of Interest Statement We confirm that the manuscript has been read and approved by all named authors and that there are no other persons who satisfied the criteria for authorship but are not listed. We further confirm that the order of authors listed in the manuscript has been approved by all of us. We confirm that we have given due consideration to the protection of intellectual property associated with this work and that there are no impediments to publication, including the timing of publication, with respect to intellectual property. In so doing, we confirm that we have followed the regulations of our institutions concerning intellectual property. We understand that the corresponding author is the sole contact for the editorial process (including editorial manager and direct communications with the office). He is responsible for communicating with the other authors about progress, submissions of revisions, and final approval of proofs. We confirm that we have provided a current, correct email address which is accessible by the corresponding author.

Novelty Statement The electrical, magnetic, structural, and spectroscopic properties of the prepared Er-substituted Mg-Zn nanoferrites have been investigated, as has electrical conductivity in dc. Now getting dynamic results requires interpretation and thermostats, thermal sensor motors, and transformer applications.

References

1. C.R. Kalaiselvan, S.S. Laha, S.B. Somvanshi, T.A. Tabish, N.D. Thorat, N.K. Sahu, Manganese ferrite (MnFe2O4) nanostructures for cancer theranostics. Coord. Chem. Rev. **473**, 214809 (2022). https://doi.org/10.1016/j.ccr.2022.214809

2. P.B. Kharat, S.B. Somvanshi, P.P. Khirade, K.M. Jadhav, Induction heating analysis of surface-functionalized nanoscale $CoFe_2O_4$ for magnetic fluid hyperthermia toward noninvasive cancer treatment. ACS Omega. **5**(36), 23378–23384 (2020). https://doi.org/10.1021/acsomega.0c03332
3. S.B. Somvanshi, P.B. Kharat, T.S. Saraf, S.B. Somwanshi, S.B. Shejul, K.M. Jadhav, Multifunctional nano-magnetic particles assisted viral RNA-extraction protocol for potential detection of COVID-19. Mater. Res. Innovations **25**, 3 (2021). https://doi.org/10.1080/14328917.2020.1769350
4. S.B. Somvanshi, S.R. Patade, D.D. Andhare, S.A. Jadhav, M.V. Khedkar, P.B. Kharat, P.P. Khirade, K.M. Jadhav, Hyperthermic evaluation of oleic acid coated nano-spinel magnesium ferrite: enhancement via hydrophobic-to-hydrophilic surface transformation. J. Alloys Compd. **835**, 155422 (2020). https://doi.org/10.1016/j.jallcom.2020.15
5. S.A. Jadhav, S.B. Somvanshi, S.S. Gawali, K. Zakade, K.M. Jadhav, Rare earth-doped mixed Ni–Cu–Zn ferrites as an effective photocatalytic agent for active degradation of Rhodamine B dye. J. Rare Earths. **7**, 004 (2023). https://doi.org/10.1016/j.jre.2023.03.004
6. L.I. Jianhui, D.U. Wenbo, L.I. Shubo, Zhaohui WANG, Effect of aging on microstructure of Mg-Zn-Er alloys. J. Rare Earths. **27**, 1042–1045 (2009). https://doi.org/10.1016/S1002-0721(08)60385-3
7. L.I. Shu-bo, D.U. Xian, D.U. Wen-bo, Hot deformation behaviours and processing maps of Mg-Zn-Er alloys based on Gleeble-1500 hot compression simulation. Trans. Nonferrous Met. Soc. **26**, 3123–3134 (2016). https://doi.org/10.1016/S1003-6326(16)64444-8
8. R. Shabadi, M. lonescu, M. Jeandin, Richard and Tara Chandra, C. Microstructure and Corrosion Behavior of Extruded Mg-Zn-Er. Mater. Sci. Forum **941**, 1766–1771 (2018). https://doi.org/10.4028/www.scientific.net/MSF.941.1766
9. S.B. Somvanshi, S.A. Jadhav, S.S. Gawali, K. Zakde, K.M. Jadhav, Core-shell structured superparamagnetic Zn-Mg ferrite nanoparticles for magnetic hyperthermia applications. J. Alloys Compd. **947**, 169574 (2023). https://doi.org/10.1016/j.jallcom.2023.169574
10. S.R. Patade, D.D. Andhare, S.B. Somvanshi, S.A. Jadhav, Mangesh V. Khedkar, K.M. Jadhav. Self-heating evaluation of superparamagnetic MnFe2O4 nanoparticles for magnetic fluid hyperthermia application towards cancer treatment. Ceram. Int. **46**(16), 25576–25583 (2020). https://doi.org/10.1016/j.ceramint.2020.07.029
11. H.R. Bakhseshi-Rad, E. Hamzah, A. Fereidouni-Lotfabadi, M. Daroonparvar, M.A.M. Yajid, M. Mezbhul-Islam, M. Kasiri-Asgarani, M. Medraj, Microstructure and bio-corrosion behavior of Mg-Zn and Mg-Zn-Ca alloys for biomedical applications. Corros. Mater. **65**, 1178–1187 (2014). https://doi.org/10.1002/maco.201307588
12. H. Liang, S.-L. Chen, Y.A. Chang, A thermodynamic description of the Al-Mg-Zn system. Metall Mater Trans A Phys Metall Mater Sci. **28**, 1725–1734 (1997). https://doi.org/10.1007/s11661-997-0104-8
13. S. Wasiur-Rahman, M. Medraj, Critical assessment and thermodynamic modeling of the binary Mg-Zn, Ca-Zn and ternary Mg-Ca-Zn systems. Metall. trans**. 17**, 847–864 (2009). https://doi.org/10.1016/j.intermet.2009.03.014
14. S.B. Somvanshi, P.B. Kharat, M.V. Khedkar, K.M. Jadhav, Hydrophobic to hydrophilic surface transformation of nano-scale zinc ferrite via oleic acid coating: magnetic hyperthermia study towards biomedical applications. Ceram. Int. **46**(6), 7642–7653 (2020). https://doi.org/10.1016/j.ceramint.2019.11.265
15. S.B. Somvanshi, M.V. Khedkar, P.B. Kharat, K.M. Jadha, Influential diamagnetic magnesium (Mg2+) ion substitution in nano-spinel zinc ferrite ($ZnFe_2O_4$): thermal, structural, spectral, optical and physisorption analysis. Ceram. Int. **46**(7), 8640–8650 (2020). https://doi.org/10.1016/j.ceramint.2019.12.097
16. J. Miettinen, Thermodynamic description of Cu-Mg-Ni and Cu-Mg-Zn systems. Calphad. **32**, 389–398 (2008). https://doi.org/10.1016/j.calphad.2008.03.005
17. S. Spigarelli, M. EI Mehtedi, Constitutive equations in creep of Wrought Mg-Zn alloys.Mat.sci.and Eng. A. **527**, 126–131 (2009). https://doi.org/10.1016/j.msea.2009.07.062
18. X. GU, Y. Zheng, S. Zhong, T. Xi, J. Wang, W. Wang, Corrosion of,and celluiar responses to Mg-Zn-Ca bulk metallic glasses. Biomaterials. **31**, 1093–1103 (2010). https://doi.org/10.1016/j.biomaterials.2009.11.015
19. T. Prosek, Persson, Dan. Stoulil, Jan. Thierry, Dominique. Composition of corrosion products formed on Zn-Mg, Zn-Al and Zn-Al-Mg coatings in model atmospheric conditions. Corros. Sci. **86**, 231–238 (2014). https://doi.org/10.1016/j.corsci.2014.05.016
20. G. Shao, V. Varsani, Z. Fan, Thermodynamic modeling of the Y-Zn and Mg-Zn-Y systems. calphad. **30**, 286–295 (2006). https://doi.org/10.1016/j.calphad.2006.03.005
21. C.C. Kammerer, S. Behdad, L. Zhou, F. Betancor, M. Gonzalez, B. Boesl, Y.H. Sohn, kinetics, Diffusion. mechanical properties and crystallographic characterization of intermetallic compunds in the Mg-Zn binary system. Intermetallic. **67**, 145–155 (2015). https://doi.org/10.1016/j.intermet.2015.08.001
22. C.O. Brubaker, Z.K. Liu, A computational thermodynamic model of the Ca-Mg-Zn system. J. Alloys Compd. **370**, 114–122 (2004). https://doi.org/10.1016/j.jallcom.2003.08.097
23. N. Venkatesh, N.H. Kumar, S. Goud, ... T.A. Babu, N.V.K. Prasad, FTIR, optical, electrical and magnetic properties of SM3+ doped MG nano ferrites. Biointerface Res. Appl. Chem. **11**(6), 15037–15050 (2021). http://dx.doi.org/10.21203/rs.3.rs-227009/v1
24. S.K. Das, Y.M. Kim, T.K. Ha, I.H. Jung, Investigation of anisotropic diffusion behavior of Zn in hcp Mg and interdiffusion coefficients of intermediate phases in Mg-Zn system. Calphad. **42**, 51–58 (2013). https://doi.org/10.1016/j.calphad.2013.07.002
25. M.A. Rahman, M.T. Islam, M.S.J. Singh et al., Synthesis and characterization of Mg–Zn ferrite based flexible microwave composites and its application as SNG metamaterial. Sci. Rep. **11**, 7654 (2021). https://doi.org/10.1038/s41598-021-87100-6
26. A. Irshad, M. Zulfiqar, H.M. Ali, N. Shahzadi, H.H. Abd El-Gawad, C. Chokejaroenrat, C. Sakulthaew, F. Anjum, M. Suleman, Co-substituted Mg–Zn spinel nanocrystalline ferrites: synthesis, characterization and evaluation of catalytic degradation efficiency for colored and colorless compounds, Ceramic International. Ceram. Int. **48**(20), 29805–29815 (2022). https://doi.org/10.1016/j.ceramint.2022.06.241
27. R. TholkappiyanK, Vishista, Combustion synthesis of Mg–Er ferrite nanoparticles: Cation distribution and structural, optical, and magnetic properties. Mater Sci Semicond Process. **40**, 631–642 (2015). https://doi.org/10.1016/J.MSSP.2015.06.076
28. correlation of physical properties with Yttrium content, Ali, M.A., Khan, M.N.I., Chowdhury, FUZ. et al. Yttrium-substituted Mg–Zn ferrites. J Mater Sci: Mater Electron **30**, 13258–13270 (2019). https://doi.org/10.1007/s10854-019-01689-z
29. A. Humbe, J.S. Kounsalye, S.B. Somvanshi, A. Kumar, K.M. Jadhav, Cation distribution, magnetic and hyperfine interaction studies of Ni–Zn spinel ferrites: role of Jahn Teller ion (Cu^{2+}) substitution. Mater. Adv. **1**, 880–890 (2020)
30. V.A. Bharati, S.B. Somvanshi, A.V. Humbe, V.D. Murumkar, V.V. Sondur, K.M. Jadhav, Influence of trivalent Al–Cr co-substitution on the structural, morphological and Mössbauer properties of nickel ferrite nanoparticles. J. Alloys Compd. **821**, 153501 (2020). https://doi.org/10.1016/j.jallcom.2019.153501
31. P. Lianga, T. Tarfa, J.A. Robinson, S. Wagner, P. Ochin, M.G. Harmelin, H.J. Seifert, H.L. Lukas, F. Aldinger, Experimental investigation and thermodynamic calculation of the Al-Mg-Zn system. Thermochim. Acta. **314**, 87–110 (1998). https://doi.org/10.1016/S0040-6031(97)00458-9
32. P. Ghosh, M. Medraj, Critical assessment and thermodynamic modeling of Mg-Zn,Mg-Sn,Sn-Zn and Mg-Sn-Zn systems.

Calphad. **36**, 28–43 (2012). https://doi.org/10.1016/j.calphad.2011.10.007
33. S.S. Parh, G.T. Bae, D.H. Kang, I.H. Jung, K.S. Shin, N.J. Kim, Microstructure and tensile properties of twin-roll cast Mg-Zn-Mn-Al alloys. Scr. Mater. **57**, 793–796 (2007). https://doi.org/10.1016/j.scriptamat.2007.07.013
34. Z. Zhang, A. Couture, A. Luo, investigation of the properties of Mg-Zn-Al alloys. Scr. Mater. **39**, 45–53 (1998). https://doi.org/10.1016/S1359-6462(98)00122-5
35. E.A. Menezes, A.F. Oliveira, C.J. Franca, G.B. Souza, A.R.A. Nogueira, Bioaccessibility of Ca,Cu,Fe,Mg,Zn,and crude protein in beef,pork and chicken after thermal processing. Sci. Total Environ. **240**, 75–83 (2018). https://doi.org/10.1016/j.foodchem.2017.07.090
36. N.H. Kumar, D. Ravinder, A. Edukondalu, Effect of Ce^{3+} ion doped Ni-Zn ferrites: Structural, optical and low temperature magnetic properties. Chin. J. Phys. **81**, 171–180 (2023). https://doi.org/10.1016/j.cjph.2022.11.019
37. D.S. YIN, E.L. ZHANG, S.Y. ZENG, Effect of Zn on mechanical property and corrosion property of extruded Mg-Zn-Mn alloy. Trans. Nonferrous Met. Soc. **18**, 763–768 (2008). https://doi.org/10.1016/S1003(08)60131-4
38. G. Khalil, M. Gouterman, S. Ching, C. Costin, L. Coyle, S. Gouin, E. Green, M. Sadilek, R. Wan, J. Yearyean B. Zeleow, Synthesis and spectroscopic characterization of Ni,Zn,Pd and Pt tetra (pentafluorophenyl)po rpholactone with comparisons to Mg,Zn,Y,Pd and Pt metal complexes of tetra(pentafiuorophenyl)porphine. J. Porphyr. Phthalocyanines. **06**,135–145 (2002). https://doi.org/10.1142/S108842460200018X
39. H. Huang, H. Kato, C. Chen, Z. Wang, G. Yuan, The effect of nanoquasicrystals on mechanical properties of as-extruded Mg-Zn-Gd alloy. Mater. Lett. **79**, 281–283 (2012). https://doi.org/10.1016/j.matlet.2012.04.018
40. S.B. Somvanshi, S.A. Jadhav, M.V. Khedkar, P.B. Kharat, S.D. More, K.M. Jadhav, Structural, thermal, spectral, optical and surface analysis of rare earth metal ion (Gd3+) doped mixed Zn–Mg nano-spinel ferrites. Ceram. Int. **46**(9), 13170–13179 (2020). https://doi.org/10.1016/j.ceramint.2020.02.091
41. A. Srinivasan, Y. Huang, C.L. Mendis, C. Blawert, K.U. Kainer, N. Hort, Investigation on microstructures, mechanical and corrosion properties of Mg-Gd-Zn alloys. Mater. Sci. Eng: A. **595**, 224–234 (2014). https://doi.org/10.1016/j.msea.2013.12.016
42. V. Ludhiya, N. Hari D. kumar, A. Ravinder, Edukondalu, Structural, optical, dielectric and magnetic properties of Nd^{3+} ion substituted Ni-Mg-Cu spinel ferrites. Inorg. Chem. Commun. **150**, 110558 (2023). https://doi.org/10.1016/j.inoche.2023.110558
43. B. Somvanshi, V.D. Murumkar, K.M. Jadhav, Influential incorporation of RE metal ion (Dy3+) in yttrium iron garnet (YIG) nanoparticles: magnetic, electrical and dielectric behaviour. Ceram. Int. **46**(10), 15372–15378 (2020). https://doi.org/10.1016/j.ceramint.2020.03.081
44. H.S. Brar, J. Wong, M.V. Manuel, Investigation of the mechanical and degradation properties of Mg-Sr and Mg-Zn-Sr alloys for use as potential biodegradable implant materials. J Mech Behav Biomed Mater. **7**, 87–95 (2012). https://doi.org/10.1016/j.jmbbm.2011.07.018
45. S. Zhang, G.Y. Yuan, C. Lu, W.J. Ding, The relationship between (Mg, Zn_3)3RE phase and 14H-LPSO phase in Mg-Gd-Y-Zn-Zr alloys solidified at different cooling rates. J. Alloys Compd. **509**, 3515–3521 (2011). https://doi.org/10.1016/j.jallcom.2010.12.136
46. B. Baburao, N.H. Kumar, A. Edukondalu, M.V. Narayana, D. Ravinder, optical, DC electrical, thermo-electric, dielectric and magnetic properties of $Mg_{0\cdot8}Zn_{0\cdot2}Gd_xFe_{2-x}O_4$ nanoparticles synthesised by citrate-gel auto combustion method. Inorg. Chem. Commun. **148**, 110355 (2023). https://doi.org/10.1016/j.inoche.2022.110355
47. F. Guo, L. Fang, X. Zhao, Y. Li, H. Cai, Effects of content and distribution of Zn and Gd on formation ability of phase and W phase in Mg-Zn-Gd-Zr alloy. J. Alloys Compd. **862**, 158543 (2021). https://doi.org/10.1016/j.jallcom.2020.158543
48. C. Platzer-Bjorkman, T. Torndahl, A. Hultqvist, A. Kessler, M. Edoff, Optimization of ALD-(Zn,Mg)O buffer layers and (Zn,Mg)O/Cu(In,Ga)Se_2 interfaces for thin film solar cells.Thin Solid Films. **515**, 6024–6027 (2007). https://doi.org/10.1016/j.tsf.2006.12.047
49. H.S. Jang, K.M. Kim, B.J. Lee, Modified embedded-atom method intermatomic potentials potentials for pure Zn and Mg-Zn binary system. Calphad. **60**, 200–207 (2018). https://doi.org/10.1016/j.calphad.2018.01003
50. G. Graf, P.S. Erdely, P. Staron, S. Peter. A. Stark, F.M. Martin, H. Clemens, T. Klein, Quench rate sensitivity of age-hardenable Al-Zn-Mg-Cu alloys with respect to the Zn/Mg ratio: an in situ SAXS and HEXRD study. Acta Mater. **227**, 117727 (2022). https://doi.org/10.1016/j.actamat.2022.117727
51. H. Wang, C. Zhao, Y. Chen, L.I. Jianan, X. Zhang, Electrochemical property and in vitro degradation of DCPD-PCL composite coating on the biodegradable Mg-Zn alloy. Mater. Lett. **68**, 435–438 (2012). https://doi.org/10.1016/j.matlet.2011.11.029
52. N.H. kumar, D. Ravinder, A. Edukondalu, Synthesis, structural, antimicrobial activity and dielectric properties of Ce^{3+}-doped Ni–Zn nano-ferrites, Appl. Phys. A **128**, 978 (2022). https://doi.org/10.1007/s00339-022-06096-6
53. Y. Chen, Y. Song, S. Zhang, J. Li, H. Wang, C. Zhao, X. Zhang, Effect of fluoride coating on in vitro dynamic degradation of Mg-Zn alloy. Mater. Lett. **65**, 2568–2571 (2011). https://doi.org/10.1016/j.matlet.2011.05.108
54. N.P. Zaksas, V.A. Gerasimov, G.A. Nevinsky, Simultaneous determination of Fe,P,Ca,Mg,Zn,and Cu in whole blood by two-jet plasma atomic emission spectrometry.Talanta. **80**, 2187–2190 (2010). https://doi.org/10.1016/j.talanta.2009.10.046
55. N.H. Kumar, D. Ravinder, T. Anil Babu, N. Venkatesh, S. Swathi, N.V. Krishna Prasad, Development of Cu^{2+} substituted Ni–Zn ferrite nano-particles and their high-temperature semiconductor behaviour. J. Indian Chem. Soc. **99**, 3 (2022). https://doi.org/10.1016/j.jics.2022.100362
56. T. Koizumi, M. Egami, K. Yamashita, E. Abe, Platelet precipitate in an age-hardening Mg-Zn-Gd alloy. J. Alloys Compd. **752**, 407–411 (2018). https://doi.org/10.1016/j.jallcom.2018.04.136
57. D. Wang, J. Zhang, J. Xu, Z. Zhao, W. Cheng, Ci. Xu, Microstructure and corrosion behavior of Mg-Zn-Y-Al alloys with long-period stacking ordered structures.J. Magnes. Alloy. **2**, 78–84 (2014). https://doi.org/10.1016/j.jma.2014.01.008
58. E. Sumalatha, N.H. kumar, A. Edukondalu, D. Ravinder, Effect of La^{3+} ion doped Co-Zn nano ferrites: structural, optical, electrical and magnetic properties. Inorg. Chem. Commun. **146**, 110200 (2022). https://doi.org/10.1016/j.inoche.2022.110200
59. G. Graf, P. Spoerk-Erdely, P. Staron, A. Stark, F.M. Martin, H. Clemens, T. Klein, Quench rate sensitivity of age-hardenable Al-Zn-Mg-Cu alloys with respect to the Zn/Mg ratio:An in situ SAXS and HEXRD study. Acta Materialia. **227**, 117727 (2022). https://doi.org/10.1016/j.actamat.2022.117727